ELSEVIER

Journal of Nuclear Materials 247 (1997) 258–264

journal of nuclear materials

Section 7. Oxide systems

Thermodynamics of the U–O and Zr-systems and application to analysis of fuel liquefaction during severe accidents in light water reactors

D.R. Olander *, Wei-E Wang

Department of Nuclear Engineering, University of California, Berkeley, CA 94720-1730, USA

Abstract

Severe accident modeling requires knowledge of the heat effects accompanying simultaneous dissolution of UO_2 and fusion of Zircaloy to form the U–Zr–O melt. Estimation of the enthalpy changes must rely chiefly on data from the U–O and Zr–O binary systems. The partial molar enthalpies of oxygen in the pure liquid metals are determined by application of Sieverts' law. The Sieverts' law constant is obtained by deriving the complete relationship between the oxygen pressure, the O/M ratio of the solid or liquid phase and temperature from the pure metal M to the dioxide MO_2. This assessment utilizes the integral constraint involving the Gibbs free energy of formation of the compound MO_C and the variation of the oxygen pressure p, over the entire composition range. Once the p–C–T relationship has been established, the enthalpy changes on dissolving UO_2 and αZr(O) into the U–Zr–O melt are computed. The heat effects of fuel/cladding dissolution in a severe accident are applied in a liquefaction model based on kinetic control by the available heat from fission product decay. In addition to the portion of the decay heat reaching the inner cladding surface, the rate of melting of the cladding depends on heat flow to its outer surface from steam oxidation or radiation from other parts of the core. Depending on the relative importance of these two heat inputs to the cladding, time to melting is from 100 to 400 s and the fraction of the fuel dissolved varies from 5 to 20%. © 1997 Elsevier Science B.V.

1. Introduction

Liquefaction of UO_2 by molten Zircaloy is one of the signal events in a severe fuel damage accident in a light-water reactor. Considerable effort by several laboratories has been devoted to understanding the kinetics of this process. The accident at the Three Mile Island nuclear reactor highlighted the importance of the chemical interactions between fuel, cladding, fission products, structural alloys and coolant at very high temperatures in understanding such events. Of central interest is the reaction of molten Zircaloy cladding with UO_2 fuel, which leads to fuel 'liquefaction' at temperatures nearly 1000°C lower than the melting point of pure UO_2. This system involves chiefly the elements U, Zr and O, but despite considerable activity concerning the kinetics of the interaction [1–5], the data on the thermodynamics of the ternary U–Zr–O system at temperatures where Zr is liquid have not been substantially advanced since Politis' measurement of the isothermal sections of the ternary phase diagram at 2000°C [6]. He also proposed a pseudo-binary UO_2–Zr(O) phase diagram which was later corrected by Skokan [7] and most recently by Hayward and George [8]. However, it is not possible to extract the heat effects of the Zr(L)–UO_2 reaction from these data. Analysis of the high-temperature fuel-cladding reaction must therefore rely on application of the much more extensive thermochemical database of the U–O and Zr–O binary systems.

2. Thermodynamics of the U–O and Zr–O binary systems

The objectives are twofold. First to critically assess the p–C–T information for the U–O and Zr–O systems,

* Corresponding author. Tel.: +1-510 642 7055; fax: +1-510 643 9685.

PII S0022-3115(97)00052-4

where p is the oxygen pressure, C is the O/M ratio of the condensed phase and T is the temperature. Second, to characterize the dissolution equilibria of O_2 in the liquid metals, with emphasis on the enthalpy of solution, which is the quantity needed for the application to severe accident analyses.

Oxidation reactions are expressed by

$$M + \frac{C}{2}O_2 = MO_C.$$

The major tool in the assessment is the Gibbs free energy integral constraint, which can be written as

$$\Delta G_f^\circ(MO_{C_i}) = \tfrac{1}{2}\int_0^{C_i} \Delta\overline{G}\,dC, \tag{1}$$

where $\Delta G_f^\circ(MO_{C_i})$ is the Gibbs free energy of formation of the oxide at the phase boundary denoted by C_i. When $C_i = 2$, the free energy of formation is that of the stoichiometric oxide.

$$\Delta\overline{G} = RT \ln p = \Delta\overline{H} - T\Delta\overline{S} \tag{2}$$

is the oxygen potential and $\Delta\overline{H}$ and $\Delta\overline{S}$ are the relative partial molar enthalpy and relative partial molar entropy of oxygen in MO_C, respectively.

Kubaschewski [9] has made extensive use of the integral constraint of Eq. (1) and Wang and Olander have extended applications to M–H_2 and M–N_2 systems [10,11].

Oxygen dissolution in the liquid metals is described by Sieverts' law, which is assumed to apply up to the terminal solubility:

$$\frac{1}{\gamma_O} = \frac{C}{\sqrt{p_L}} = \frac{C_1}{\sqrt{p_{L-ox}}}, \tag{3}$$

where γ_O is the activity coefficient of oxygen dissolved atomically in the melt, p_L is the oxygen pressure in equilibrium with the melt with $C = O/M$ ratio, C_1 is the terminal solubility of oxygen in the liquid metal and p_{L-ox} is the equilibrium oxygen pressure in the two-phase liquid + oxide region of the phase diagram.

2.1. Application to UO_C, $0 \le C \le 2$, $1400 \le T \le 2600$ K

The assessed phase diagram for UO_{2+x} with superimposed oxygen isobars has been presented by Naito [12]. A similar analysis for UO_{2-x} reported by Wang and Olander [13] is shown in Fig. 1. The dotted lines represent oxygen isobars, or the p–C–T relationship, and their determination is outlined here. In addition to the terminal solubility and the lower phase boundary of the hypostoichiometric oxide, the data available for this assessment include oxygen pressures in the UO_{2-x} solid solution and in the two-phase region below 2600 K. The literature sources of these data are given in Ref. [13].

Since the Gibbs free energy of formation of UO_2 is well-established, the appropriate form of Eq. (1) is broken

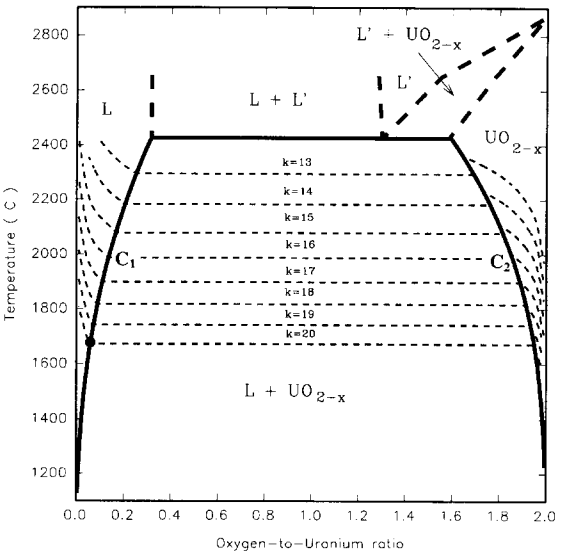

Fig. 1. Phase diagram of the U–O system for $O/U < 2$. Oxygen isobars are indicated by the index k in p (atm) $= 10^{-k}$.

up into components over the liquid metal phase, the two-phase region and the oxide solid solution:

$$\frac{\Delta G_f^\circ(UO_2)}{RT} = \tfrac{1}{2}\left[\int_0^{C_1} \ln p_L\,dC + (C_2 - C_1)\ln p_{L-ox} + \int_{C_2}^{2} \ln p_{ox}\,dC\right], \tag{4}$$

where C_2 is the O/U ratio at the lower phase boundary of UO_{2-x} and p_{ox} is the oxygen pressure of this solid solution.

If Sieverts' law is obeyed for oxygen dissolution in the liquid metal, p_L in Eq. (4) can be obtained from Eq. (3). Although the terminal solubility of oxygen in U(L) is still a disputed matter, the right hand side of Eq. (4) is most sensitive to the two-phase pressure p_{L-ox}. Consequently, this quantity is expressed by

$$\ln p_{L-ox} = A - B/T \tag{5}$$

and the best values of the constants A and B are determined by fitting to Eq. (4) at a series of temperatures between 1400 to 2600 K. The oxygen pressure of the hypostoichiometric oxide can be taken from either Blackburn's model [14] or the representation of Lindemer and Besmann [15] without significantly affecting the outcome of the fitting procedure. The values of A and B in Eq. (5) so determined are compared to two independent measurements in Table 1.

The numbers in Table 1 show very good agreement between the two experimentally-determined two-phase oxygen pressures and that determined by Eq. (4) using the ensemble of the other data for the U–O system. The good agreement also shows that Sieverts' law in the form of Eq.

Table 1
Constants in Eq. (6) for the two-phase liquid–oxide region of the U–O system

Source	A	B (K)
Markin [16]	20.09	129900
Ackermann et al. [17]	20.93	129400
Integral constraint	20.57	129700

(3) is at least not inconsistent with the remainder of the database when used in Eq. (4), although the first term on the right hand side of this equation contributes little to the sum. The Gibbs free energy of solution of oxygen in liquid uranium that results from the second equality of Eq. (3) is

$$RT \ln \gamma_O = -106 + 0.014T \text{ kcal/mol}. \quad (6)$$

The dotted lines in Fig. 1 show the oxygen isobars determined by the above procedure.

2.2. Application to ZrO_C, $0 \le C \le C_2$, $2338 \le T \le 2600$ K

Fig. 2 shows the assessed Zr–O phase diagram reported by Abriata et al [18] with oxygen isobars constructed by Wang and Olander [13]. This binary system is obviously more complex than the U–O system. However, if attention is restricted to temperatures above 2338 K, the phase diagram is qualitatively similar to that of the U–O system between 1400 and 2600 K: it contains a substoichiometric oxide, a liquid metal and a two-phase liquid + oxide region in between. A significant quantitative difference between the two systems is the high terminal solubility of oxygen in liquid Zr compared to that in liquid U. The large solubility in the Zr–O system calls into question the applicability of Sieverts' law over the entire liquid metal region. Special attention is paid to this potential pitfall in Ref. [19] and in the following analysis.

Although the Gibbs free energy of formation of stoichiometric ZrO_2 is as accurately known as any other formation free energy in the Zr–O system, it is separated from the liquid region by the wide cubic oxide single-phase zone and the intervening two-phase region. The single-phase cubic oxide contributes substantially to the integral in Eq. (1) if the upper limit is taken as two. The available oxygen potential data in the cubic oxide solid solution [20] are bunched close to the upper phase boundary in the V-shaped region at the low-temperature end of the phase region, leaving the p–C–T relation near the lower phase boundary along C_2 poorly characterized. On the other hand, there are reliable measurements of the oxygen pressure in the adjacent L + ox region, also above 2338 K [21]. Hence, the integral constraint is useful only when applied up to the boundary C_2 in Fig. 2.

No measurements of the oxygen pressure in equilibrium with oxygen-containing liquid Zr have been reported. In this region, Sieverts' law is assumed but verification of its applicability is needed because of the high terminal solubility. This is accomplished by calculating the free energy of formation along the terminal solubility curve C_1 in two ways. The first is a direct calculation, by integrating the oxygen potential assuming Sieverts' law with p_L expressed by Eq. (3):

$$\Delta G_f^\circ(ZrO_{C_1}) = \frac{RT}{2}\int_0^{C_1} \ln p_L \, dC$$

$$= \frac{RT}{2} C_1\left(\ln p_{L-ox} - \tfrac{1}{2}\right). \quad (7)$$

The second application of the integral constraint starts from Ackermann's free energy of formation at the lower phase boundary of the cubic oxide (C_2) and subtracts the contribution from the two-phase region, using p_{L-ox} data from the same source. This yields

$$\Delta G_f^\circ(ZrO_{C_1}) = \Delta G_f^\circ(ZrO_{C_2}) - \frac{RT}{2}(C_1 - C_2)\ln p_{L-ox}. \quad (8)$$

The free energies of formation along C_1 calculated from Eqs. (7) and (8) are within ~ 2 kcal/mol of each other over the entire temperature range considered. This good agreement not only verifies the accuracy of Ackermann's measurements but justifies the applicability of Sieverts' law to oxygen dissolution in liquid Zr even for O/Zr ratios > 1. With Sieverts' law established, the Gibbs free energy of oxygen dissolution in Zr(L) is given by

$$RT \ln \gamma_O = -111 + 0.021T \text{ kcal/mol}, \quad (9)$$

which is quite close to that deduced for O in U(L), Eq. (6).

The oxygen isobars in the L and L + ox regions of Fig. 2 were determined by the preceding analysis. More de-

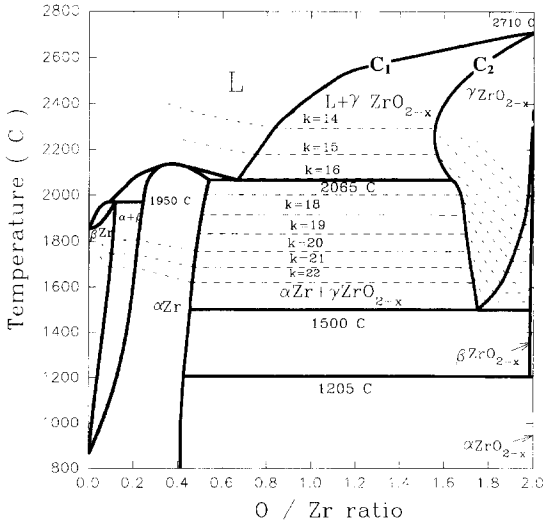

Fig. 2. Phase diagram of the Zr–O system. Oxygen isobars are indicated by the index k in p (atm) = 10^{-k}.

tailed considerations at lower temperatures [13] produced isobars involving the solid forms of Zr. These are also shown in Fig. 2.

3. Application to severe fuel-damage analysis

One of the most dramatic events in a loss-of-coolant accident in a water reactor occurs when the Zircaloy cladding melts. Prior to melting, the cladding has absorbed oxygen by reaction with residual steam in the core. The mass of Zircaloy in the core is so much larger than the mass of steam that the likelihood of steam-starvation is high. When the metal–water reaction runs out of steam, the ZrO_2 scale that had formed on the cladding surface dissolves in the remaining metal, producing Zr with dissolved oxygen, or αZr(O) [22]. According to Fig. 2, the αZr(O) phase can have O/Zr ratios as large as 0.4. The melting temperature of the oxygen-containing metal is between 1800 and 2100°C, depending on the oxygen content.

Fig. 3 shows the fuel-cladding interface prior to melting of the cladding(top) and during the fuel liquefaction stage(bottom). In the latter, fission-product decay heat supplies the reaction enthalpies of UO_2 dissolution and melting of the αZr(O) cladding. This stage ends when the cladding has completely melted and the U–Zr–O melt slumps to a lower elevation in the core. Most efforts to model this process have been based on diffusion control of the kinetics [1–5]. However, a case can be made that heat supply, not species diffusion, controls the rate of dissolution of fuel and cladding [23].

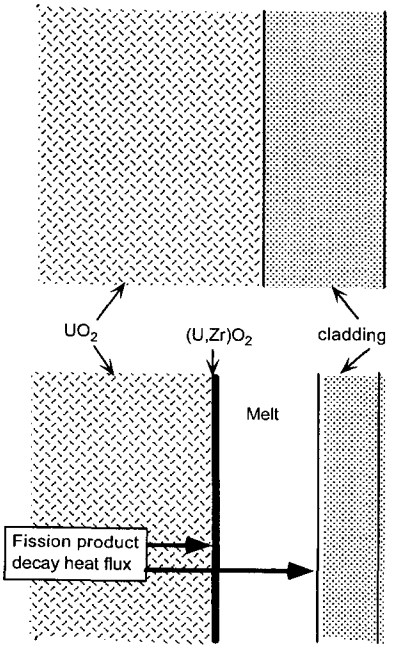

Fig. 3. Development of U–Zr–O melt between fuel and cladding driven by fission product decay heat flux.

3.1. Fuel and cladding dissolution limited by the decay heat supply

The heat-limited model is based on the endothermicity of the fuel and cladding dissolution reactions coupled with the specified heat flow from the fuel due to decay of the fission products. It leads to the heat balance

$$\dot{Q} = \dot{M}_U \Delta H_U + \dot{M}_{Zr} \Delta H_{Zr}, \tag{10}$$

where $\dot{Q}$ is fission-product decay heat flux at the fuel-cladding interface, W/cm^2; $\dot{M}_U$, $\dot{M}_{Zr} = UO_2$ and αZr(O) dissolution fluxes, $mol/cm^2\,s$; ΔH_U, ΔH_{Zr} are enthalpies of UO_2 and αZr(O) dissolution in the melt, J/mol.

To utilize Eq. (10), the moles of U and Zr per unit area in the melt, M_U and M_{Zr} respectively, must be related to each other. Because diffusion and convection of U, Zr and O in the melt are very efficient, phase equilibrium between the melt and a thin layer of mixed (U, Zr)O_2 on the fuel surface is established. The Zr-enriched layer is thin because Zr^{4+} ions are very immobile in the ceramic lattice of the fuel and over the time scale of the accident, zirconium does not significantly penetrate the fuel. How equilibrium of the melt and this thin layer on the fuel relates M_U to M_{Zr} is based on the ternary phase diagram shown in Fig. 4 for a typical cladding melting temperature of 2000°C. The melt composition is located at the intersection P of the UO_2–αZr(O) material-balance join (since these two solids supply the melt constituents) with the liquidus line. The composition of the thin mixed oxide layer on the fuel surface is connected to the melt composition by the equilibrium tie line shown schematically as the dashed line PS in Fig. 4. Although these tie lines are not known, the location of point S is not important because the mixed-oxide layer is thin and so does not contribute to the material balances.

In terms of the quantities of fuel and cladding dissolved, the ternary mole fractions of the melt at point P are

$$p_U = \frac{M_U}{3M_U + (1+n)M_{Zr}},$$

$$p_{Zr} = \frac{M_{Zr}}{3M_U + (1+n)M_{Zr}} \tag{11}$$

and $p_O = 1 - p_U - p_{Zr}$. In Eq. (11), n is the O/Zr ratio of the solid αZr(O).

In the vicinity of point P, the liquidus is satisfactorily represented by the linear form

$$p_{Zr} = b - a p_U, \tag{12}$$

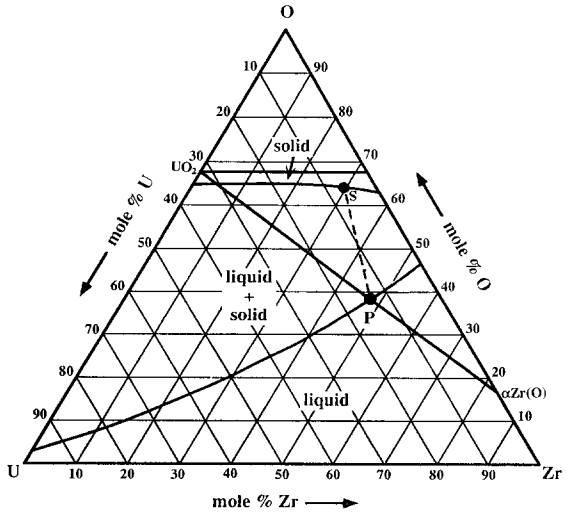

Fig. 4. Ternary section of the U–O–Zr phase diagram at 2000°C [6]. Point P is on the liquidus; point S is on the solidus. Dashed line PS is a hypothetical equilibrium tie line.

where $a = 0.44$ and $b = 0.54$. Substituting Eq. (11) into Eq. (12) yields

$$M_{Zr} = KM_U, \quad \text{where } K = \frac{3b - a}{1 - b(1 + n)}. \tag{13}$$

3.2. Enthalpies of fuel and cladding dissolution

The final quantities needed for application of Eq. (10) are the dissolution enthalpies. These quantities cannot be approximated simply as the heats of fusion of the solids because of changes in the strong metal–oxygen interactions upon conversion from the solid to the melt phase. Following the approach used in Ref. [24], each dissolution process (i.e., $UO_2 \rightarrow$ U–Zr–O melt and αZr(O) $\rightarrow$ U–Zr–O melt) is treated as the isothermal addition of the solid containing 1 mol of metal plus the associated oxygen into a large quantity of melt of specified composition $U_yZr_{1-y}O_m$. The composition of the melt does not change by adding the solid phase, so the heat effects are due to partial molar enthalpy changes, denoted by ΔH_U and ΔH_{Zr} for UO_2 and αZr(O), respectively.

Fig. 5 shows the two dissolution processes broken into steps for which the enthalpy changes can be computed. Dissolution of the oxygen-containing solid metal is shown in the bottom half of the diagram. In step (A), removal of oxygen from the solid Zr–O solution incurs the enthalpy change

$$\Delta H_A = -nh_{O,Zr(s)}, \tag{14}$$

where $h_{O,Zr(s)} = -135$ kcal/mol [25] is the average enthalpy of solution of one half a mole of O_2(g) in αZr(O). As in the case of Zr(L), oxygen dissolution in Zr(s) is assumed to obey Sieverts' law, which implies that the heat of solution of oxygen is independent of oxygen concentration.

Step (B) is simple melting of Zr(s), for which

$$\Delta H_B = h_M, \tag{15}$$

where $h_M = 5.4$ kcal/mol is the heat of fusion of pure Zr.

Step (C) consumes $\frac{1}{2}$ mol of the O_2 liberated in step (A) in forming the liquid metal with the final oxygen content

$$\Delta H_C = mh_{O,Zr(L)}, \tag{16}$$

where, according to Eq. (9), $h_{O,Zr(L)} = -111$ kcal/mol is the heat of solution of $\frac{1}{2}$ mol of oxygen gas in liquid Zr.

In step (D), the oxygen-to-metal ratio of the zirconium melt is the same as that of the final mixed-metal melt, so the interaction involved here is approximately that of adding 1 mol of Zr to a large quantity of U–Zr alloy:

$$\Delta H_D = \overline{h_{Zr}} - h_{Zr}^\circ = \alpha y^2, \tag{17}$$

where y is the mole fraction of uranium in the melt on an oxygen-free basis. $\alpha = -7$ kcal/mol is the interaction parameter of the U–Zr alloy, in which non-ideality is approximated by regular solution theory [26].

Step (E) adds the remaining oxygen gas to the melt:

$$\Delta H_E = (n - m)h_{O,M(L)}, \tag{18}$$

where $h_{O,M}$ is the heat of solution of $\frac{1}{2}$ mol of O_2 in the melt. Because the analysis at the beginning of the paper demonstrated Sievert's-law behavior for both U(L) and Zr(L), the melt should behave similarly, so

$$h_{O,M(L)} = yh_{O,U(L)} + (1 - y)h_{O,Zr(L)}, \tag{19}$$

where $h_{O,U(L)} = -106$ kcal/mol is the heat of solution of $\frac{1}{2}$ mol O_2 in liquid uranium (see Eq. (6)).

Adding the five contributing enthalpy changes gives the heat absorbed by the process:

$$\Delta H_{Zr} = h_M - n\left(h_{O,Zr(s)} - h_{O,M(L)}\right) + \alpha y^2. \tag{20}$$

The second term in this equation reflects the difference in the binding energy of oxygen in Zr(s) and in the melt. ΔH_{Zr} does not depend on the O/M ratio of the melt (m) because the heat of solution of oxygen is independent of the oxygen concentration (Sievert's law). As an example, if $n = 0.2$ and $y = 0$, $\Delta H_{Zr} = 10.2$ kcal/mol, which is nearly twice as large as the heat of fusion of pure Zr. The effect is due to the stronger oxygen binding in the solid compared to that in the liquid.

The heat of dissolution of UO_2 in the melt is computed with the aid of the individual steps starting from the solid fuel at the top of Fig. 5. In step (F), UO_2 is decomposed to U(L) and O_2(g), for which the enthalpy change is the negative of the standard heat of formation of UO_2:

$$\Delta H_F = -\Delta H_f^\circ(UO_2) = -(-260) \text{ kcal/mol}. \tag{21}$$

The mole of O_2 liberated in this step is divided into two parts. The first part is added to U(L) to form a U–O

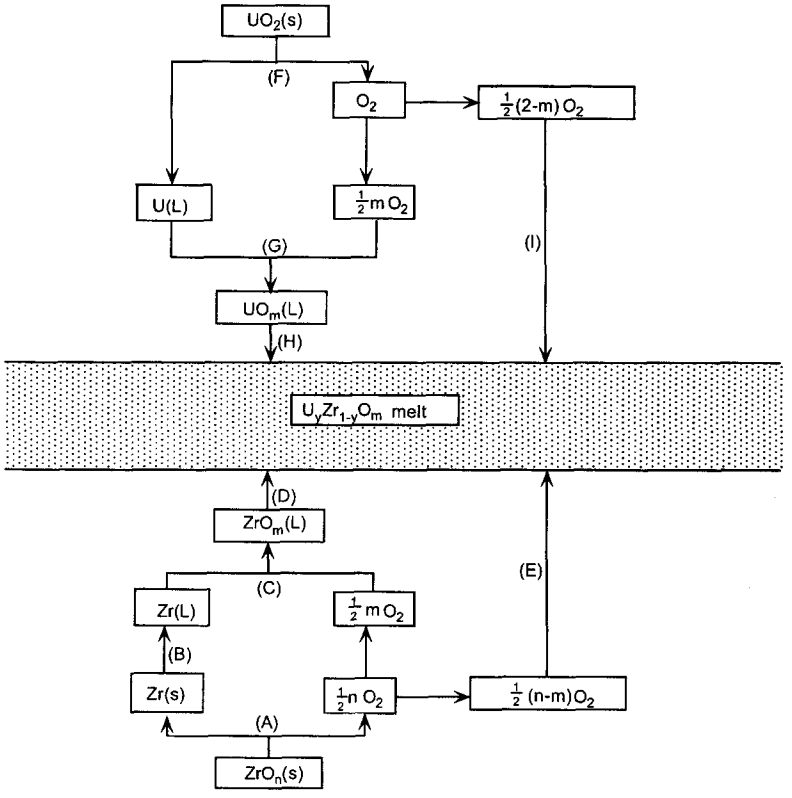

Fig. 5. Dissolution of fuel and cladding in U–Zr–O melt.

melt with the same oxygen-to-metal ratio as the final mixed-metal melt(step (G)). The remainder of the 1 mol of O_2 is added to the melt (step (I)).

In step (G), $\frac{1}{2}$ mol of O_2(g) are added to U(L), which results in the following enthalpy change:

$$\Delta H_G = mh_{O,U(L)}. \tag{22}$$

In step (H), the oxygen-to-metal ratio of the uranium melt is the same as that of the final mixed-metal melt, so the interaction involved here is approximately that of adding 1 mol of U to a large quantity of U–Zr alloy:

$$\Delta H_H = \overline{h_U} - h_U^o = \alpha(1-y)^2, \tag{23}$$

where the interaction parameter is the same as in step (D) above.

In step (I), the remaining oxygen is added to the melt, leading to the enthalpy change:

$$\Delta H_I = (2-m)h_{O,M(L)}. \tag{24}$$

The heat absorbed in dissolving 1 mol of UO_2 into the melt is the sum of steps (F)–(I):

$$\Delta H_U = -\Delta H^f_{UO_2} + mh_{O,U(L)} + \alpha(1-y)^2 + (2-m)h_{O,M(L)}. \tag{25}$$

For the melt composition at point P in Fig. 4, $m = 0.64$ and $y = 0.21$. The αZr(O) composition in this figure corresponds to $n = 0.2$. Using these values in Eq. (25) gives $\Delta H_U = 38$ kcal/mol, which is more than twice the heat of fusion of UO_2.

Substituting Eq. (13) into Eq. (10), solving for the cladding dissolution flux and dividing by the molar density of liquid Zr gives the speed of melting of the cladding:

$$v_{clad} = \frac{\dot{Q}}{\rho_{Zr}(\Delta H_U/K + \Delta H_{Zr})}. \tag{26}$$

The decay heat flux at the fuel-cladding interface needed to produce the ~ 1 K/s temperature rise rate estimated in the TMI reactor accident is ~ 1.2 W/cm^2 [23]. For $n = 0.2$, Eq. (13) gives $K = 3.0$. The density of liquid Zr is $\rho_{Zr} \sim 0.07$ mol/cm^3. Using these figures and the dissolution enthalpies previously determined in Eq. (26) gives a cladding melting speed of $\sim 2 \times 10^{-4}$ cm/s. For a typical cladding thickness of 0.8 mm, the time required to melt the cladding is ~ 400 s. During this period, the quantity of fuel dissolved in the melt is

$$M_U = \frac{M_{Zr}}{K} = \frac{0.08 \times 0.07}{3.0} = 2 \times 10^{-3} \frac{\text{mol U}}{\text{cm}^2}.$$

For a pellet diameter of 9 mm, this quantity of dissolved fuel corresponds to ~ 20% of the original fuel pellet.

4. Summary

Two significant features of the heat-limited melt liquefaction model have been omitted in the analysis presented here. The first is the presence of a heat flux incident on the outer surface of the cladding. This added heat source causes cladding melting from the outside. Inclusion of this effect reduces the cladding melt-through time to ~ 100 s [23]. This reduction in contact time between the melt and the fuel also reduces the quantity of fuel dissolved.

The second phenomenon considered in Ref. [23] is reduction of the interior of the fuel pellet from UO_2 to UO_{2-x} by solid state oxygen diffusion during the dissolution process. The additional oxygen source reduces the solubility of uranium in the melt. Together with the decreased contact time, the fraction of the original fuel pellet that dissolves before melt relocation is only $\sim 5\%$.

Thus, the initial cladding melting process does not appear to be chiefly responsible for the substantial quantity of molten fuel produced in the TMI accident. The molten mass probably originated from the collapse of fuel stacks that became unstable once the cladding melted off. Subsequent decay heating of the resulting uncoolable rubble pile probably accounted for most of the molten fuel mass.

References

[1] P. Hofmann, H. Uetsuka, A.N. Wilhelm, E.A. Garcia, Dissolution of Solid UO_2 by Molten Zircaloy and Its Modeling, IAEA/NEA Proc. on Severe Accidents in Nuclear Power Plants, Sorrento, IAEA-SM 296/1, 1988, pp. 3–17.
[2] K.T. Kim, D.R. Olander, J. Nucl. Mater. 154 (1988) 102.
[3] P.J. Hayward, I.M. George, J. Nucl. Mater. 208 (1994) 35.
[4] M.S. Veshchunov, A.M. Volchek, J. Nucl. Mater. 188 (1992) 177.
[5] M.S. Veshchunov, P. Hofmann, J. Nucl. Mater. 209 (1994) 27.
[6] C. Politis, Untersuchungen im Dreistoffsystem Uran-zircon-Sauerstoff, Forschungszentrum Karlsruhe Report No. KfK 2167, 1975.
[7] A. Skokan, High Temperature Phase Relations in the U–Zr–O System, 5th Int. Meeting on Thermal Nuclear Reactor Safety, Karlsruhe, Germany, Sept. 1984.
[8] P.J. Hayward, I.M. George, Dissolution of UO_2 in molten zircaloy. Part 4: Phase evolution during dissolution and cooling, J. Nucl. Mater., to be published.
[9] O. Kubaschewski,d C.B. Alcock, Metallurgical Thermochemistry, 5th Ed. (Pergamon, Oxford, 1979).
[10] W.-E. Wang, D.R. Olander, J. Am. Ceram. Soc. 78 (1995) 3323.
[11] W.-E. Wang, D.R. Olander, J. Alloys Compounds 224 (1995) 153.
[12] K. Naito, N. Kamegashira, Adv. Nucl. Sci. Technol. 9 (1976) 99.
[13] W.-E. Wang, D.R. Olander, J. Am. Ceram. Soc. 76 (1993) 1242.
[14] P.E. Blackburn, J. Nucl. Mater 46 (1973) 244.
[15] T.B. Lindemer, T.M. Besmann, J. Nucl. Mater. 130 (1985) 473.
[16] T.L. Markin, Chem. Engin. Progr. Symp. Ser. 63 (1967) 43.
[17] R.J. Ackermann, E.G. Rauh, M.S. Chandrasekharaiah, J. Phys. Chem. 73 (1969) 762.
[18] J.P. Abriata, J. Barces, R. Versaci, Bull. Alloy Phase Diagrams 7 (1986) 116.
[19] W.-E. Wang, D.R. Olander, J. Alloys Compounds 228 (1995) 31.
[20] E.G. Rauh, S.P. Garg, High Temp. Sci. 14 (1981) 121.
[21] R.J. Ackermann, S.P. Garg, E.G. Rauh, High Temp. Sci. 11 (1979) 199.
[22] D.R. Olander, Nucl. Eng. Design 148 (1994) 253.
[23] D.R. Olander, Nucl. Eng. Design 162 (1996) 257.
[24] D.R. Olander, W.-E. Wang, J. Nucl. Mater. 223 (1995) 28.
[25] G. Boureau, P. Gerdanian, J. Phys. Chem. Solids 45 (1984) 141.
[26] T. Ogawa, T. Iwai, J. Less Common Met. 170 (1991) 101.